Oxygen impurities link bistability and magnetoresistance in organic spin valves

Ilaria Bergenti[a], Francesco Borgatti*[a], Marco Calbucci[b], Alberto Riminucci[a], Raimondo Cecchini[c], Patrizio Graziosi[a], Donald MacLaren[d], Angelo Giglia[e], Jean Pascal Rueff[f], Denis Céolin[f], Luca Pasquali[e,g], Valentin Dediu[a]*

a.CNR-ISMN, via Gobetti 101, 40129 Bologna, Italy

b.Institute of Molecular Science (ICMol) Catedrático José Beltrán Martínez 2 46980 Paterna Spain

c.MDM Laboratory, IMM-CNR, Via C. Olivetti 2, 20864 Agrate Brianza, MB, Italy

d.SUPA, School of Physics and Astronomy, University of Glasgow, Glasgow G12 8QQ

e.IOM-CNR, s.s. 14, Km. 163.5 in AREA Science Park, Basovizza, 34149 Trieste, Italy

f.Synchrotron SOLEIL, Saint-Aubin, BP 48,F-91192 Gif-sur-Yvette Cedex, France

g.Dipartimento di Ingegneria E. Ferrari, Via Vivarelli 10, 41125 Modena, Italy, Department of Physics, University of Johannesburg, P.O. Box 524, Auckland Park 2006, South Africa

KEYWORDS. organic spintronics, spin valve, spin transport, impurity levels, oxygen dopants

ABSTRACT.

Vertical cross-bar devices based on manganite and cobalt injecting electrodes and metal-quinoline molecular transport layer are known to manifest both magnetoresistance and electrical bistability. The two effects are strongly interwoven, inspiring new device applications such as electrical control of the magnetoresistance and magnetic modulation of bistability. To investigate the full device functionality, we first identify the mechanism responsible for electrical switching by associating the electrical conductivity and the impedance behavior with chemical states of buried layers obtained by in operando photoelectron spectroscopy. These measurements revealed that a significant fraction of oxygen ions migrates under voltage application, resulting in a modification of the electronic properties of the organic material and of the oxidation state of the

hysteresis and their electrical resistance is dependent on the intensity and polarity of a pre-applied "writing" voltage pulse; the resistance change is non-volatile, i.e it persists after the voltage pulse has ended. [1] Recent experiments indicate that, in devices involving spin polarised injectors and metal-quinoline transport layers, in addition to RS, magnetoresistance (MR) occurs.[3-6] Interestingly the two phenomena are strongly correlated: MR can be turned "on" and "off" as well as smoothly tuned between a number of non-volatile states depending on the device resistive state obtaining a full electrical control of MR.[3, 4] This 'multifunctionality' is tantalizing for the development of new devices,[7, 8] with potential applications in multibit nonvolatile data

the organic layer,[19] the latter is explained by the formation of locally highly conductive channels (filaments) and is related to redox effects.[20, 21]

In such a complex scenario, the correlation of electrical bistability with MR has obviously created expectations for an additional way of investigating the transport behavior, both for spin and charge properties. Two hypotheses were considered in literature to account for both effects, none of them proven experimentally. In one case it is speculated that MR originates from spin-dependent electron tunneling into highly conductive filamentary paths.[22] Alternatively, a tunnel barrier has been suggested to form [5] at the FM/organic interface, with the barrier being reversibly

electrode (inset of **Figure1**). An AlO_x tunnel barrier (2nm thick) was deposited between the Gaq_3 and Co layers to minimize the penetration of Co atoms into the organic layer. [23-25] Gaq_3 was considered instead of the well known Alq_3 [26] because it provides similar magnetoelectric behavior, but it allows to decouple the spectroscopic signal originating from the AlO_x barrier and from the organic layer. Samples were prepared *ex-situ* using Channel Spark ablation deposition for LSMO,[27] thermal evaporation for Gaq_3 and Al and electron beam evaporation for Co layer. AlO_x was obtained by exposing the Al layer to a partial pressure of O_2. Transmission electron

7 nm) allowed us to investigate deep regions within a working device and to study the effects of the resistive switching on the top electrode, the underlying organic layer and the interfaces with the barrier layer. Devices presented a retention time [7] that greatly surpassed the HAXPES and XAS measurement timescale, ensuring that the observed spectroscopic signatures are unambiguously associated with specific resistance states. XAS measurements were performed across the Co $L_{2,3}$, O-K and C-K absorption edges at the BEAR beamline (Elettra-Trieste). [30] Spectra are acquired in total electron yield mode, by measuring the sample drain current, and they are normalized to the beam flux by using a clean gold sample as reference. HAXPES

Figure 1a shows the typical hysteretic behavior of the current-voltage characteristic, which depends on the polarity of the applied voltage[4] (with respect to the grounded Co top electrode). Initially, devices are in a low resistance state ($R_{IRS}(0.1V) \sim 25\ K\Omega$) that we call IRS; the I-V characteristic is marked as (1). From the IRS, the device can be set to a high resistance state (HRS) by the application of a sufficiently negative voltage. In Figure 1a the device in the HRS reaches higher $R_{HRS} \sim 1M\Omega$ at 0.1 V and is marked as (2). This state is non-volatile and in order to set the device to a low-resistance-state (LRS marked as (3) with $R_{LRS}(0.1V) \sim 5\ k\Omega$ at 0.1 V)

Figure 1 (a) I–V curves of LSMO/ Gaq_3/AlO_x/Co ultra thin device at RT displaying the bistability effect. Inset shows the device structure (b) Negative magnetoresistive response for two different resistive states measured at 100K: LRS (R=5kΩ, MR 8%) and HRS (R=125kΩ, MR 2%) measured at V_{bias}=-0.1V.

To gain insight into the difference in transport between different resistive states, we carried out impedance spectroscopy (V_{AC}=0.01V V_{DC}=-0.1V). The impedance was modeled as a parallel RC loop with a series resistance, R_S (**Figure 2a**).

Figure 2 (a)Impedance spectra of two different resistive states. The line is the fit to the equivalent circuit of a R

In each impedance spectrum, the impedance magnitude showed a plateau at low frequencies and decreased above a cut off frequency. Typically, for two different resistive states an almost identical capacitance of C= 2.36 10^{-9}F was found. This value is in agreement with the geometrical value calculated using a relative permittivity of $_r$= 4 as expected for a metal quinoline layer,[40] indicating that the RS was not caused by an extraneous capacitive mechanism at the electrode/organic layer interface and can therefore not be responsible for the conductivity of the individual device states. The series resistance was very low for both states (Rs ~1KΩ) and was attributed to the electrodes whilst the parallel resistance varied during the transition in

describes conduction in organic semiconductors as reported in numerous fundamentals studies.[46] [47, 48] Most works were based on thick organic films and involved a high number of hopping events. At the opposite end, for very thin film, direct tunneling is considered as the dominant mode of transport. Since our devices are made of organic films of intermediate thickness, the approach of Xu *et a*[49], which focusses on transport through a small number of hopping events, is best suited to describe our results (see SI1). Hopping involving up to three localized states fits the experimental data well as shown by continuous line in figure 2b,c. Hopping distances of only a few nanometres are then estimated, indicating that a thinning of the layers' thickness with

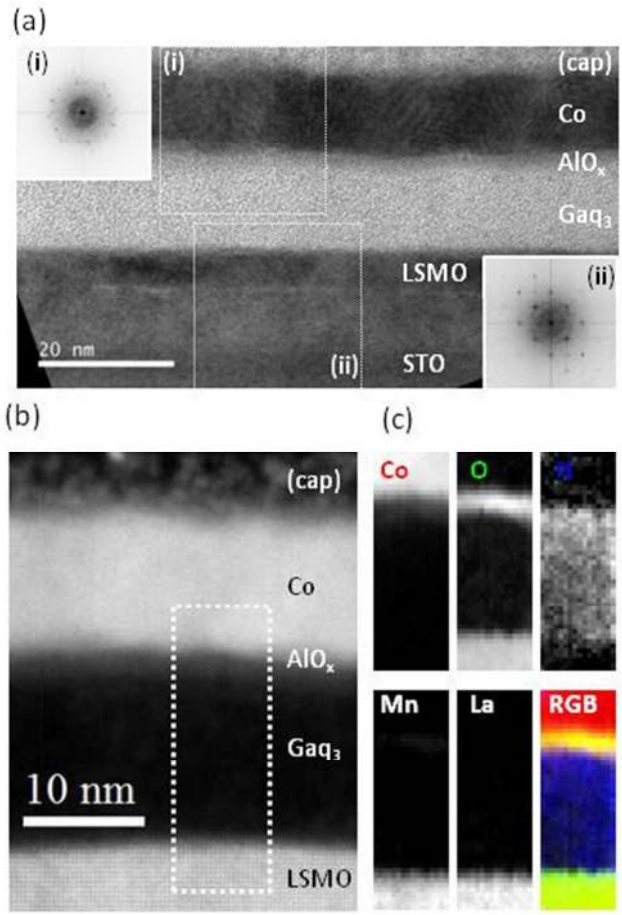

Figure 3 (a) Cross sectional TEM image of a typical device with the layer compositions indicated. Fourier transforms (inset) of the regions labeled (i) and (ii) indicate that the Co layer is polycrystalline and the LSMO and STO have a clear epitaxial relationship. (b)Electron energy loss spectroscopic analysis of a typical device: Dark field STEM image with major layers labeled. Heavier elements appear darkest and the region used for EELS analysis is indicated. (c) Composition maps showing the distribution of elements within the analysed region, each panel indicating the relative strength of background-subtracted EELS signal. The final panel is a red-green-blue composite of the Co, O and N signals.

In operando X-ray Photoelectron Spectroscopy (HAXPES) and X-ray Absorption Spectroscopy (XAS) provide a straightforward evidence of processes setting bistability. XAS spectra of the Co $L_{2,3}$ thresholds are presented in **Figure 4a** and do not reveal significant differences between the HRS and LRS. Both spectra are characteristic of predominantly metallic cobalt and lack pronounced satellite features that would indicate substantial cluster formation [51] or complete oxidation [52], although a weak shoulder is present on the high-energy side of both peaks that suggests the formation of a thin oxide layer, in agreement with the EELS data (SI2).

Figure 4(a)

The interpretation of O K-edge spectra, shown in **figure 4b**, is more complex because contributions arise from both AlO_x and Gaq_3 layers but an important result is that there are clear changes between the HRS and LRS. The spectra are dominated by a broad peak centered at E=546 eV (labeled 'C') and there are two satellites, at E= 539.8 eV ('B') and E= 537 eV ('A'). Previous studies of amorphous AlO_x layers [54] and Gaq_3 [55, 56] allow feature A to be attributed to AlO_x (see SI3). Recent paper [57] on AlO_x based RS devices uses the sharpness of this satellite peak as an indicator of the presence of oxygen vacancies. Indeed, it has been noted elsewhere that AlO_x

higher (lower) oxidation state,[61] indicating that in the HRS the Al experiences increased oxygenation and a slightly more inhomogeneous chemical environment. The increase of oxygenation in HRS is confirmed by the relative percentage of the peak associated to the AlO_x with respect to the total area that is 78% while in LRS is 74%. (See **Table 1**)

Tab 1 Al 1s assignments for AlO_x and metallic Al and the relative contribution to the total peak area in the three resistive states. Each contribution is fitted by using a Guassian line shape.

Both O K-edge and Al1s analysis indicate a difference in the Al oxidation state between the LRS and HRS. We propose that the HRS, set by the application of a negative bias to the LSMO contact, is obtained by trapping of O_2

We turn now to the organic molecule. It is well established from theoretical calculations [62, 63] that in metal quinoline complexes the highest occupied molecular orbital (HOMO) is located on the phenoxideside of the quinolinol ligands, whereas the lowest unoccupied molecular orbital (LUMO) is found on the pyridyl side; the central metal ion (Ga) contributes negligibly to the density of states (DOS). Thus, it may be expected that any possible variations to the electronic configuration of the molecule during RS are most likely to produce a sizeable effect on the N1s or C1s HAXPES spectra. The C1s core levels HAXPES spectra for IRS, HRS and LRS are shown in **figure 5b**.

Figure 5

LRS. Lines represent the three components and red lines the curve fit. Inset: HAXPES N1s spectra for IRS and HRS

They results from three main components corresponding to three bonding environments for carbon in the structure of the 8-quinolinol ligand (C–C bonds, C–H bonds, and C–X bonds where X stands for oxygen or nitrogen) and it is consistent with previous investigations [25] of similar samples. During the fitting process, the area ratio for the C–C, C–H, and C–X components was kept 1:3:5, in agreement with their ratios in the complex. The binding energies of all three components do not change between the IRS and the LRS but in the HRS increase by 0.25 eV, which is generally a signature of an oxidation process (i.e. removal of electronic charge).

and feature more structured contributions with respect to experimental data, indicating that extrinsic broadening due to complex molecular configuration is expected to dominate in devices. By a qualitative comparison of the measured and calculated spectra in neutral and positively charged states, the narrower experimental lineshape of the broad feature centered at 289 eV in HRS indicates a partial presence of a Gaq_3 cations.

Figure 6 (a) X-ray absorption spectra measured across the C K absorption edge. (b)Calculated C K edge absorption spectra for neutral Gaq_3 molecule and for Gaq_3 cation obtained by a removal of an electronic charge.

Considering the Oxygen drift in and out the barrier, the reversible generation of positively charged states in Gaq

the electronic charge within the complex yields then a negatively charged oxygen molecule and a hole on the quinoline ligand. [68]

The positive charging of the organic molecules, modifying their electronic structure,[69, 70] results in a higher localization of electrons in the HOMO with respect to the neutral and negatively charged quinoline molecule. This localization of the HOMO would be unfavorable for electron hopping to a neighboring molecule and thus unfavorable for electron transport, as expected for HRS.[69] We stress that XAS and HAXPES spectroscopic investigations average all over the sample probing volume and thus changes of the electronic configuration of organic layer are not restricted to local conduction paths as expected in filamentary conduction process but involves

An important issue to take into account is the voltage regime at which bistability and MR are found. While bistability is set by applying few V to our device, MR is detectable only at small voltages (well below 1 V) which are lower than interfacial electronic barriers for the charge injection into HOMO or LUMO level.[71] Such peculiar MR voltage dependence together with the absence of Hanle effect [72] expected in case of HOMO-LUMO transport, pushed several authors [12, 36] to propose a qualitatively different picture to describe spin transport in the OSVs based on the presence of intragap localized levels.

Figure 7 Schematic representation of RS: HRS (left) and LRS (right). HRS is set by the

the organic molecules. Switching to the LRS, oxygen migrates towards the LSMO layer to leave a defective AlO_x barrier and restore the neutrality of the Gaq_3 molecule.

In our case, the MR intensity depends on the specific resistive state in which the device is put: on the basis of results above, MR is absent when a more efficient insulating AlO_x barrier is set and Gaq_3 cations are formed, while MR has its maximum value in case of defective AlO_x barrier and after oxygen ions migration into the organic layer and the formation of complexes. We expect then that AlO_x defective barrier [73] will generate a number of localized states able to promote the

switching and magnetic characteristics uniquely to oxygen variations in the LSMO electrode. [80] Our set of data do not access the interfacial LSMO layer in reason of the limited electron escape depth for Hard X-Ray photoemission, providing little access to the deep buried interface with LSMO layer. Nevertheless, our data provide a complementary interpretation of the mechanism, indicating significant modifications of the stoichiometry of the aluminum oxide barrier and substantial oxygen diffusion inside the organic layer, both factors controlling the device resistance.

4. CONCLUSIONS

In summary, we have demonstrated that resistive switching effect in LSMO/Gaq_3/AlO_x/Co

SI2:Details of EELS analysis

SI3: Supporting data for O Kedge XAS interpretation:

.

AUTHOR INFORMATION

Corresponding Author

*Phone:+39 0516398509 Fax:+39 0516398540 mail: ilaria.bergenti@cnr.it

Author Contributions

The manuscript was written through contributions of all authors. All authors have given approval to the final version of the manuscript

Funding Sources

This work is funded through the European Union Seventh Framework Programme (FP7/2007-2013) under grant agreement GA No. 263104 and COST action 15128. We thank SOLEIL and ELETTRA synchrotrons for provision of synchrotron radiation facilities at beamline GALAXIES (proposal number 20130329) and beamline BEAR (proposal number 20135188) respectively.

REFERENCES

1. Scott, J. C.; Bozano, L. D., Nonvolatile Memory Elements Based on Organic Materials.

3. Hueso, L. E.; Bergenti, I.; Riminucci, A.; Zhan, Y. Q.; Dediu, V., Multipurpose Magnetic Organic Hybrid Devices. *Advanced Materials* **2007,** *19* (18), 2639-2642.

4. Prezioso, M.; Riminucci, A.; Bergenti, I.; Graziosi, P.; Brunel, D.; Dediu, V. A., Electrically Programmable Magnetoresistance in Multifunctional Organic-Based Spin Valve Devices. *Advanced Materials* **2011,** *23* (11), 1371-1375.

5. Grünewald, M.; Homonnay, N.; Kleinlein, J.; Schmidt, G., Voltage-controlled oxide barriers in organic/hybrid spin valves based on tunneling anisotropic magnetoresistance. *Physical Review B* **2014,** *90* (20), 205208.

6. Dediu, V.; Hueso, L. E.; Bergenti, I.; Riminucci, A.; Borgatti, F.; Graziosi, P.; Newby, C.; Casoli, F.; De Jong, M. P.; Taliani, C.; Zhan, Y., Room-temperatuzUUUUh,(G)8z,(e)Lz88A,g

memristance and magnetoresistance in oxide magnetic tunnel junctions. *Nanoscale* **2015,** *7* (14), 6334-6339.

11. Sun, D.; Yin, L.; Sun, C.; Guo, H.; Gai, Z.; Zhang, X. G.; Ward, T. Z.; Cheng, Z.; Shen, J., Giant Magnetoresistance in Organic Spin Valves. *Physical Review Letters* **2010,** *104* (23), 236602.

12. Barraud, C.; Seneor, P.; Mattana, R.; Fusil, S.; Bouzehouane, K.; Deranlot, C.; Graziosi, P.; Hueso, L.; Bergenti, I.; Dediu, V.; Petroff, F.; Fert, A., Unravelling the role of the interface for spin injection into organic semiconductors. *Nat Phys* **2010,** *6* (8), 615-620.

13. Xiong, Z. H.; Wu, D.; Valy Vardeny, Z.; Shi, J., Giant magnetoresistance in organic spin-valves. *Nature* **2004,** *427* (6977), 821-824.

14. Cinchetti, M.; Dediu, V. A.; Hueso, L. E., Activating the molecular spinterface. *Nature Materials* **2017,** *16*, 507.

19. Chu, C. W.; Ouyang, J.; Tseng, J. H.; Yang, Y., Organic Donor–Acceptor System Exhibiting Electrical Bistability for Use in Memory Devices. *Advanced Materials* **2005,** *17* (11), 1440-1443.

20. Cölle, M.; Büchel, M.; de Leeuw, D. M., Switching and filamentary conduction in non-volatile organic memories. *Organic Electronics* **2006,** *7* (5), 305-312.

21. Busby, Y.; Nau, S.; Sax, S.; List-Kratochvil, E. J. W.; Novak, J.; Banerjee, R.; Schreiber, F.; Pireaux, J.-J., Direct observation of conductive filament formation in Alq3 based organic resistive memories. *Journal of Applied Physics* **2015,** *118* (7), 075501.

22. Li, B.; Yoo, J.-W.; Kao, C.-Y.; Jang, H. W.; Eom, C.-B.; Epstein, A. J., Electrical bistability and spin valve effect in a ferromagnet/organic semiconductor/ferromagnet

26. Droghetti, A.; Steil, S.; Großmann, N.; Haag, N.; Zhang, H.; Willis, M.; Gillin, W. P.; Drew, A. J.; Aeschlimann, M.; Sanvito, S.; Cinchetti, M., Electronic and magnetic properties of the interface between metal-quinoline molecules and cobalt. *Physical Review B* **2014,** *89* (9), 094412.

27. Graziosi, P.; Prezioso, M.; Gambardella, A.; Kitts, C.; Rakshit, R. K.; Riminucci, A.; Bergenti, I.; Borgatti, F.; Pernechele, C.; Solzi, M.; Pullini, D.; Busquets-Mataix, D.; Dediu, V. A., Conditions for the growth of smooth La0.7Sr0.3MnO3 thin films by pulsed electron ablation. *Thin Solid Films* **2013,** *534*, 83-89.

28. Hunt, J. A.; Williams, D. B., Electron energy-loss spectrum-imaging. *Ultramicroscopy* **1991,** *38* (1), 47-73.

33. Triguero, L.; Pettersson, L. G. M.; Ågren, H., Calculations of near-edge x-ray-absorption spectra of gas-phase and chemisorbed molecules by means of density-functional and transition-potential theory. *Physical Review B* **1998,** *58* (12), 8097-8110.

34. Bozano, L. D.; Kean, B. W.; Deline, V. R.; Salem, J. R.; Scott, J. C., Mechanism for bistability in organic memory elements. *Applied Physics Letters* **2004,** *84* (4), 607-609.

35. Waser, R.; Aono, M., Nanoionics-based resistive switching memories. *Nat Mater* **2007,** *6* (11), 833-840.

36. Tran, T. L. A.; Le, T. Q.; Sanderink, J. G. M.; van der Wiel, W. G.; de Jong, M. P., The Multistep Tunneling Analogue of Conductivity Mismatch in Organic Spin Valves. *Advanced Functional Materials* **2012,** *22* (6), 1180-1189.

41. Sebastian, P.; Lindner, F.; Walzer, K.; Lüssem, B.; Leo, K., Investigation on the origin of the memory effect in metal/organic semiconductor/metal structures. *Journal of Applied Physics* **2011,** *110* (8), 084508.

42. Nau, S.; Sax, S.; List-Kratochvil, E. J. W., Unravelling the Nature of Unipolar Resistance Switching in Organic Devices by Utilizing the Photovoltaic Effect. *Advanced Materials* **2014,** *26* (16), 2508-2513.

43. Cho, B.; Song, S.; Ji, Y.; Kim, T.-W.; Lee, T., Organic Resistive Memory Devices: Performance Enhancement, Integration, and Advanced Architectures. *Advanced Functional Materials* **2011,** *21* (15), 2806-2829.

44. Pender, L. F.; Fleming, R. J., Memory switching in glow discharge polymerized thin films.

49. Xu, Y.; Ephron, D.; Beasley, M. R., Directed inelastic hopping of electrons through metal-insulator-metal tunnel junctions. *Physical Review B* **1995,** *52* (4), 2843-2859.

50. Gobbi, M.; Golmar, F.; Llopis, R.; Casanova, F.; Hueso, L. E., Room-Temperature Spin Transport in C60-Based Spin Valves. *Advanced Materials* **2011,** *23* (14), 1609-1613.

51. Cheng, P.-Y.; Chiang, M.-R.; Chan, Y.-L.; Hsu, Y.-J.; Wang, P.-C.; Wei, D. H., Deep Co penetration and spin-polarization of C60 molecules at hybridized Co-C60 interfaces. *Applied Physics Letters* **2014,** *104* (4), 043303.

52. Telling, N. D.; van der Laan, G.; Ladak, S.; Hicken, R. J.; Arenholz, E., Evidence of a barrier oxidation dependence on the interfacial magnetism in Co/alumina based magnetic tunnel junctions.

structure spectroscopy and first principles calculations. *Journal of Applied Physics* **2012,** *112* (11), 113519.

57. Nigo, S.; Kubota, M.; Harada, Y.; Hirayama, T.; Kato, S.; Kitazawa, H.; Kido, G., Conduction band caused by oxygen vacancies in aluminum oxide for resistance random access memory. *Journal of Applied Physics* **2012,** *112* (3), 033711.

58. Tan, E.; Mather, P. G.; Perrella, A. C.; Read, J. C.; Buhrman, R. A., Oxygen stoichiometry and instability in aluminum oxide tunnel barrier layers. *Physical Review B* **2005,** *71* (16), 161401.

59. Laubender, J.; Chkoda, L.; Sokolowski, M.; Umbach, E., The influence of oxygen and air on the characteristics of organic light-emitting devices studied by in vacuo measurements. *Synthetic Metals* **2000,**

64. Kim, S. C.; Kim, J. W.; Lee, J.; Park, Y., Formation of a Ca/LiF/Alq(3) cathode for an organic light-emitting diode: Evolution of the electronic structure as studied by photoemission spectroscopy. *Journal of the Korean Physical Society* **2008,** *53* (2), 812-817.

65. DeMasi, A.; Piper, L. F. J.; Zhang, Y.; Reid, I.; Wang, S.; Smith, K. E.; Downes, J. E.; Peltekis, N.; McGuinness, C.; Matsuura, A., Electronic structure of the organic semiconductor Alq3 (aluminum tris-8-hydroxyquinoline) from soft x-ray spectroscopies and density functional theory calculations. *The Journal of Chemical Physics* **2008,** *129* (22), 224705.

66. Abdou, M. S. A.; Orfino, F. P.; Son, Y.; Holdcroft, S., Interaction of Oxygen with

71. Zhan, Y. Q.; de Jong, M. P.; Li, F. H.; Dediu, V.; Fahlman, M.; Salaneck, W. R., Energy level alignment and chemical interaction at Alq3/Co interfaces for organic spintronic devices. *Physical Review B* **2008,** *78* (4), 045208.

72. Riminucci, A.; Prezioso, M.; Pernechele, C.; Graziosi, P.; Bergenti, I.; Cecchini, R.; Calbucci, M.; Solzi, M.; Dediu, V. A., Hanle effect missing in a prototypical organic spintronic device. *Applied Physics Letters* **2013,** *102* (9).

73. Sun, X.; Gobbi, M.; Bedoya-Pinto, A.; Txoperena, O.; Golmar, F.; Llopis, R.; Chuvilin, A.; Casanova, F.; Hueso, L. E., Room-temperature air-stable spin transport in bathocuproine-based spin valves. *Nature Communications* **2013,** *4*, 2794.

74. Yu, Z. G., Impurity-band transport in organic spin valves. *Nat Commun* **2014,** *5*.

79. Galbiati, M.; Tatay, S.; Delprat, S.; Khanh, H. L.; Servet, B.; Deranlot, C.; Collin, S.; Seneor, P.; Mattana, R.; Petroff, F., Is spin transport through molecules really occurring in organic spin valves? A combined magnetoresistance and inelastic electron tunnelling spectroscopy study. *Applied Physics Letters* **2015,** *106* (8), 082408.

80. O'Shea, K. J.; MacLaren, D. A.; McGrouther, D.; Schwarzbach, D.; Jungbauer, M.; Hühn, S.; Moshnyaga, V.; Stamps, R. L., Nanoscale Mapping of the Magnetic Properties of (111)-Oriented La0.67Sr0.33MnO3. *Nano Letters* **2015,** *15* (9), 5868-5874.

TOC GRAPHIC

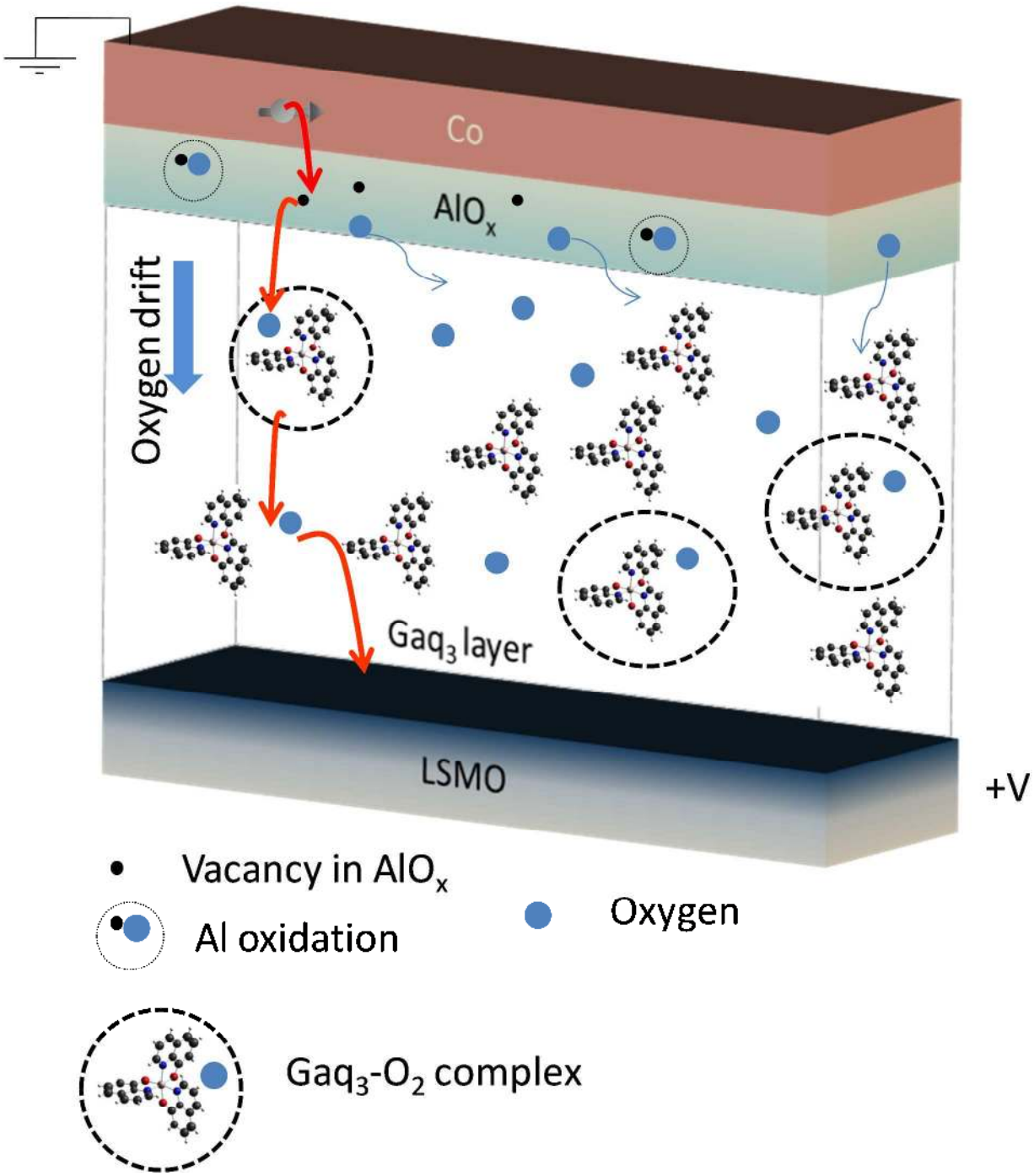
Co
AlO$_x$
Oxygen drift
Gaq$_3$ layer
LSMO
+V
Vacancy in AlO$_x$
Oxygen
Al oxidation
Gaq$_3$-O$_2$ complex

Supplementary information

S1:Voltage dependence of the hopping conductance

Figure S1, black dots, shows the differential conductance G as a function of the applied voltage in the HRS, top panel, and in the LRS, bottom panel. G is not constant, which rules out ohmic conduction. The amorphous nature of the Gaq3 and AlOx barriers indicated that charge transport could be understood in terms of the model by Xu et al. [1]. According to this model, the conductance G could be described by a voltage dependent expression in which each V^x represents a different charge transport channel:

$$Ga(V)= G_0+G_{4/3}\times V^{4/3}+G_{5/2}\times V^{5/2}$$

where G_0includes both direct and resonant tunneling, $V^{4/3}$ describes hopping across two impurity states in the amorphous insulating barrier, while $V^{5/2}$ describes hopping across 3 impurity states.In order to explain the asymmetry of G, we also introduced a linear term in V, which represents the contribution of asymmetric injection barriers from the electrodes [2]

$$G(V)= G_0+ G_{LIN}\times V+G_{4/3}\times V^{4/3}+G_{5/2}\times V^{5/2}$$

The red curves in Figure S1 represent the fit, which are in excellent agreement with the data for both resistive states. This demonstrates that the conduction mechanism is the same in both states and that what changes between the two is the number of sites across which hopping is possible.

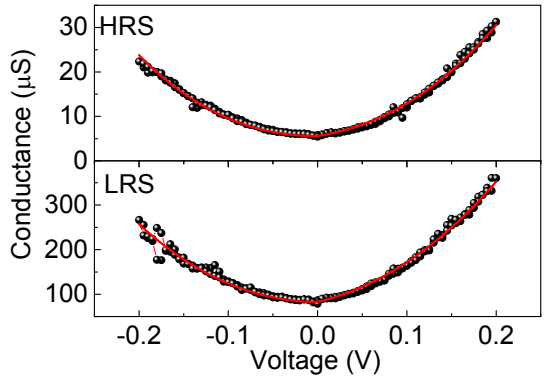

Figure S1: Differential conductance of a device at 300 K in HRS and LRS

S2:EELS analysis

Electron energy loss spectroscopy was used to assess compositional variations across the devices and typical results are presented in **Fig. S2**, the upper panels of which (b) indicate the distribution of elements within the dotted region of Fig. S2(a). The EELS signals reveal the clear laminar structure and reveal in particular the oxygen band beneath the top Co electrode that is consistent with the presence of a continuous AlO_x barrier layer. The elemental distribution as a function of depth is more clearly plotted in Fig. S2(c), which plots the integrated elemental counts within the upper panels. (Note that uneven milling during the FIB preparation has led to the thickness of the organic layer appearing wedge-like in the N signal.) Of particular note is the uniform oxygenation of the organic layer, which is implicated in the switching mechanism proposed below. Note, also, that the Co signal does not stop abruptly at the upper AlO_x interface, but tails-off across the AlOx and into the organic layer. More detailed analysis of the Co $L_{2,3}$ signal, shown in Fig. S2(d) and S2(e), indicates the trace quantities of Co within the AlO_x and organic layers to be oxidized: the concentration of oxide is too low to give rise to a strong signal in the HAXPES results described below.

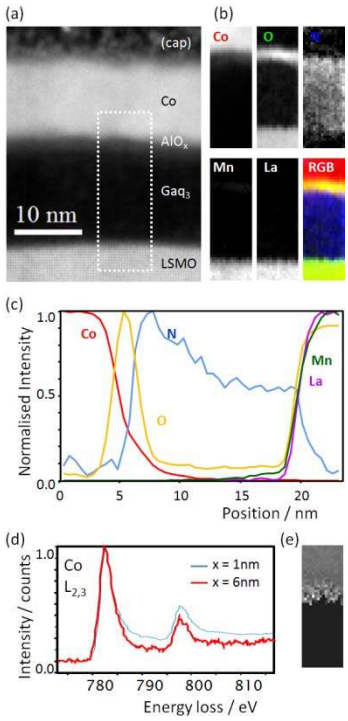

Fig. S2. Electron energy loss spectroscopic analysis of a typical device. (a) Dark field STEM image with major layers labeled. Heavier elements appear darkest and the region used for EELS analysis is indicated. (b) Composition maps showing the distribution of elements within the analysed region,

each panel indicating the relative strength of background-subtracted EELS signal. The final panel is a red-green-blue composite of the Co, O and N signals. (c) Line profiles derived from the composition maps, showing the distribution of elements across the device. Note that uneven FIB milling of the organic layer leads to the apparent wedge-shaped nitrogen profile. (d) Detail of the Co $L_{2,3}$ EELS edges taken within the electrode and at the position of the AlO_x barrier, where small quantities of oxidized Co are found. (e) A map of the change in the $L_{2,3}$ integrated intensity ratio is consistent with oxidation of the intermixed Co, within the barrier region.

S3: O Kedge XAS interpretation:

From [3] and reference therein, O K-edge lineshape for amorphous AlOx layers, as expected in our case and confirmed by TEM, is constituted by one broad peak and at least 2 low intensity features far from the main peak (ΔE1= 4.7 eV and ΔE2=10 eV). From the satellite energy position, we can associate the exact spectra position of O K-edge for AlO_x by locating the small feature at 531.3 eV as the peak at ΔE2. As consequence the peak ΔE1 is associated to peak A. The contribution of Gaq3 to O K-edge consists of a main broad peak with two satellites with separation ΔE=1.5eV associated to transition from O1s to respectively LUMO, LUMO+1 (taken from refs [4] [5]). The relative energy separation between peak B and A (Δ(B-A)= 2.8 eV) is larger than that associated to the Gaq3 satellites, making thus the association of the A peak univocally to AlO_x.

S4: XPS Al1s

Al 1s peak consists of three components that we associate to Al oxide (AlO_x) , to elemental Al and to higher oxidation states for Al, as for example Al2O3 contributions [6]. Each contribution is fitted by using a Guassian line shape. The following table summarizes the assignments and the relative contribution to the total peak area in the three resistive states.

	Assignement	Energy (eV)	FWHM	Peak area
IRS	Al-O	1561.2	1.7	62.0 %
	Al-Al	1558.6	2.5	14.5%
HRS	Al-O	1561.3	1.8	78.0%
	Al-Al	1558.6	2.0	5.5%
LRS	Al-O	1561.1	1.6	74.0%
	Al-Al	1558.6	3.1	8.1%

References

[1] Y. Xu, D. Ephron, M. R. Beasley, *Physical Review B* **1995**, 52, 2843.

[2] W. F. Brinkman, R. C. Dynes, J. M. Rowell, *Journal of Applied Physics* **1970**, 41, 1915.

[3] C. Århammar, A. Pietzsch, N. Bock, E. Holmström, C. M. Araujo, J. Gråsjö, S. Zhao, S. Green, T. Peery, F. Hennies, S. Amerioun, A. Föhlisch, J. Schlappa, T. Schmitt, V. N. Strocov, G. A. Niklasson, D. C. Wallace, J.-E. Rubensson, B. Johansson, R. Ahuja, *Proceedings of the National Academy of Sciences* **2011**, 108, 6355.

[4] T. Yokoyama, H. Ishii, N. Matsuie, K. Kanai, E. Ito, A. Fujimori, T. Araki, Y. Ouchi, K. Seki, *Synthetic Metals* **2005**, 152, 277.

[5] S. Fang, Z. Pang, Y. Du, L. Zheng, X. Zhang, F. Wang, H. Yuan, S. Han, *Journal of Applied Physics* **2012**, 112, 113519.

[6] P. Risterucci, O. Renault, C. Zborowski, D. Bertrand, A. Torres, J. P. Rueff, D. Ceolin, G. Grenet, S. Tougaard, *Applied Surface Science* **2017**, 402, 78.